PIV measurements in a turbulent wall jet over a backward-facing step in a three-dimensional, non-confined channel

Thien Duy Nguyen, Souad Harmand

PIV measurements in a turbulent wall jet over a backward-facing step in a three-dimensional, non-confined channel

Thien D. Nguyen [a,b,*], Harmand Souad [a,b]

[a] Université Lille Nord de France, F-59000 Lille, France
[b] UVHC, TEMPO, F-59313 Valenciennes, France

A study of a turbulent wall jet over a backward-facing step is especially of interest because it shows a rich phenomenon flow and a mechanism to alter the flow characteristics downstream of the step. However, studies on this flow configuration are rare. In this paper, we considered this flow configuration in a non-confined channel as the specific engineering applications of electrical rotating machines and alternator that can be found in modern wind generators of the power production industry and automobile engines. The turbulent wall jet over a backward-facing step in a non-confined wind tunnel had the jet Reynolds number of 24,100 and the step Reynolds number of 11,900. Particle image velocity (PIV) and stereoscopic PIV measurements were performed along the central plane and several cross-stream planes. Numerical simulation of the test configuration was conducted by solving the three-dimensional Reynolds Averaged Navier–Stokes (RANS) equations with the second-order closure Reynolds stress model (RSM). The mean flow fields and second-order statistical moments from the RSM simulation were compared to results that were obtained through the PIV and stereo-PIV experiments. The mean reattachment length obtained from the current configuration was much shorter than those from the backward-facing step in the plane channel. The stereo-PIV measurements in the cross-stream planes revealed a high three-dimensionality of the flow, a high population of streamwise vortice in the upper region, near the side walls and the corners formed by the side walls and the bottom wall. The obtained results also confirmed the presence of the wall-jet formation on the bottom wall.

1. Introduction

Separated flows are important in many engineering applications such as flows over airfoils at large angles of attack, flows in combustors, turbines and compressors, and flows over sedimentary dunes. To achieve a better understanding of separated flows, researchers have been attracted to study a turbulent flow over a backward-facing step (BFS), which is a geometrically simple type of separated flow. In the BFS flow configuration, an incoming flow upstream (which is usually a turbulent boundary layer developed from a plane channel or from a plane wall jet) encounters a sudden change in the vertical direction that causes the boundary layer to separate. The shear layer is generated at this step, it later reattaches on the bottom wall at a time-averaged reattachment point. Under the shear layer, a recirculation zone is formed, and the flow within is unsteady, highly three dimensional, and consists of large-scale structures of size $O(h)$, where h is the step height.

Two-dimensional BFS configuration is considered when the aspect ratio (AR) of the incoming flow, defined by the ratio of the channel width to the step height, can be assumed to be infinite. Armaly et al. [4] reported various flow regimes that are characterized by typical variations in the separation lengths versus the Reynolds numbers from 70 to 8000, the primary recirculation zone, and the flow separation downstream of the step and on both sides of the channel. Adams and Johnston [1] in their BFS study for $800 < Re_h < 40,000$ found that the reattachment and the peak pressures in the reattachment zone decrease when the upstream boundary layer increases. Driver and Seegmiller [18] and Jovic and Driver [29] performed numerical simulations and used their laser Doppler velocimetry (LDV) measurements to compare with the direct numerical simulation (DNS) of Le et al. [35]. Since the developments of the particle image velocimetry (PIV) technique [2], many studies of the BFS flow have been conducted using this technique. For instance, Scarano and Riethmuller [52], Kostas et al. [31] and Nguyen et al. [43] used their PIV experimental results on the BFS flow to study the flow dynamics and/or validate with the DNS results. Numerical calculations of the two-dimensional BFS flow using the Reynolds Averaged Navier-Stokes (RANS) approach have been investigated in So and Yuan [54] and Bischof et al. [8],

* Corresponding author at: Experimental and Computational Multiphase Flow Group, University of Michigan, Ann Arbor, Michigan 48109-2104, US.
E-mail address: thien.duy.ng@gmail.com (T.D. Nguyen).

Nomenclature

$\langle . \rangle$	time-averaged operator
ν	kinematic viscosity of air (m^2/s)
Re_j	$= U_j D_j/\nu$, jet Reynolds number
Re_h	$= U_m h/\nu$, step Reynolds number
Δt_{PIV}	PIV sampling interval (s)
D_j	cross-stream diameter of the jet (m)
h	step height (m)
k	turbulent kinetic energy (m^2/s^2)
$L_{downstream}$	streamwise length of the backward-facing step (m)
L_{jet}, L_z	streamwise inlet and spanwise lengths of the jet (m)
$L_{upstream}$	streamwise length of the wall jet (m)
u, v, w	streamwise, vertical and spanwise velocities (m/s)
u', v', w'	streamwise, vertical and spanwise fluctuating velocities (m/s)
U_j	mean jet velocity (m/s)
U_m	$U_{max}(x/h = 0)$, reference velocity (m/s)
x, y, z	streamwise, vertical and spanwise directions
X_r	reattachment length (m)
$y_{1/2}$	wall jet half-width, where $U(y_{1/2}) = 0.5U_{max}$ (m)
AR	aspect ratio (ratio of channel width and jet diameter or step height)
BFS	backward-facing step
LDA	laser Doppler anemometry
RANS	Reynolds averaged Navier–Stokes
RSM	the second-order closure Reynolds stress model

where the authors validated various turbulence models and effects of their constants to the results. Arnal and Friedrich [5] used their large-eddy simulations (LES) to study the stress terms in the separation and reattachment regions and show the presence of topological flow patterns for turbulent shear flows.

Although there have been numerous studies of the two-dimensional BFS flow, few numerical simulations and experiments on the three-dimensional BFS have been performed. In the early 1990s, subsequent visualizations of flow with AR = 10 indicated that the spanwise uniformity of the mean flow was significantly distorted within a short streamwise distance from the step [47]. These authors found that the secondary flow, which was generated by the streamwise vortices near the side walls, diminished the spanwise uniformity of the time-mean flow properties. Nie and Armaly [45] in their LDV measurements of the three-dimensional BFS flow (AR = 8) for $100 < Re_h 8000$ showed that the three-dimensional results at the centre of the test section were slightly lower in the fully turbulent flow regime. Moreover, the size of the reverse flow region adjacent to the side wall and the flat wall remained constant or diminished. Piirto et al. [50] performed PIV measurements and RANS simulations of the square BFS flow (AR = 4.7) at $Re_h = 12,000$, 21,000 and 55,000, and showed a clear difference in their root-mean-square (r.m.s.) fluctuating velocity and Reynolds stress profiles versus the DNS of Le et al. [35] due to the side wall effect. In this study, however, no direct measurement of the velocity in the cross-stream plane to illustrate the streamwise flow characteristics near the side walls was presented.

Although there have been numerous studies of BFS flow configurations mainly dealing with the turbulent boundary layer developed from the flat plane and in the confined channel, i.e., the top fixed wall, few studies have been concerned with the BFS flow in a non-confined channel, i.e., an open top surface and a turbulent wall jet upstream. Wall jets are of great engineering importance in many applications, such as defrosters in automobiles, aero engines, and gas turbines [21]. In addition, a wall jet can be found in cooling and ventilation systems, i.e., it is a fundamental idealization of a refrigerated air curtain [7] and it is found in separation control over air plane wings [10]. Most studies of turbulent wall jets have usually been performed in a two-dimensional configuration, and they are measured at a downstream region, where the flow obtains self-similar characteristics [34,65,21,16]. Engineering applications of a wall jet, however, commonly encounter three-dimensional effects due to having a low aspect ratio, having irregular surface shapes that make the flows highly unsteady, and being complex.

A study of a turbulent wall jet over a backward-facing step is especially of interest because it shows a rich phenomenon flow and a mechanism to alter the flow characteristics downstream of the step. However, studies on this flow configuration are rare, i.e. Jacob et al. [28] and Nait Bouda et al. [37] according to the authors knowledge. Jacob et al. [28] performed acoustic and aerodynamic measurements of the turbulent wall jet over a BFS in an open channel (AR = 20) at the jet Reynolds number of 210,000 and the step Reynolds number of 258,000. Their LDA results showed that the reattachment length was much shorter than that of the BFS flow with the plane channel upstream. Nait Bouda et al. [37] performed LDA measurements on a two-dimensional configuration (AR = 35), and a two-dimensional Reynolds stress model simulation at the step Reynolds number of 7600. Their results showed that the turbulent wall jet strongly modified the flow structure downstream of the BFS.

In this paper, we considered a configuration of a turbulent wall jet over a backward-facing step as the specific engineering applications of electrical rotating machines and alternator that can be found in modern wind generators of the power production industry and automobile engines. The configurations in these applications are the case of flows between a rotor and a stator, in which the stator can be confined or non-confined surfaces as shown in Fig. 1. The phenomenon of separation and reattachment of the non-confined configuration, which has not been studied in the literature, is the main contribution of this study. Experimental and numerical studies on heat transfer of this configuration have been presented in Lancial et al. [33], where the authors used an infrared camera and a hot-wire to visualize a temperature map and measure velocity. In this paper, we aim to investigate the flow characteristics of a turbulent wall jet over a backward-facing step in a non-confined

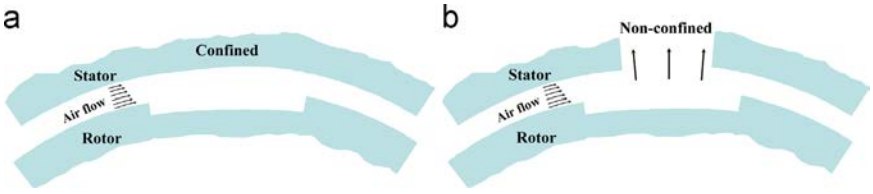

Fig. 1. Configuration of flows between a rotor and a stator with the (a) confined and (b) non-confined surfaces.

channel with a low aspect ratio (AR = 8.1). The jet Reynolds number based on the mean jet inlet velocity and the jet diameter was 24,100. The step Reynolds number based on the velocity $U_{max}(x/h = 0)$ and the step height was 11,900. In this study, two-dimensional two-component (2D2C) PIV and 2D3C stereoscopic PIV measurements along the central plane and several cross-stream planes were obtained. Numerical simulation of the test configuration was performed by solving the three-dimensional Reynolds averaged Navier–Stokes (RANS) equations. Turbulence calculations were performed using a second-order closure Reynolds stress model (RSM). The experimental rig and PIV experimental setup are presented in Section 2. Details of the numerical simulation are described in Section 3. Results of the PIV measurements and comparisons versus the RSM simulation are presented in Section 4 for the inlet region, the wall jet region and the backward-facing step region. In Section 4, the presence of longitudinal streamwise vortices in the upper region, near the side walls, and at the corners of the side walls and the bottom wall are discussed, and the conclusions are presented in Section 5.

2. Experimental setup and PIV measurements

Experimental setup and details of a turbulent wall jet over a backward-facing step in a non-confined wind tunnel are shown in Fig. 2. In the present experiment, air was supplied at room temperature by a centrifugal blower and was guided into a 3-m-long wind tunnel with a $0.17 \times 0.4\ m^2$ cross section. The air flow was driven through a conditioning section, which was composed of a honeycomb, a screen and a contraction to obtain a uniform air jet flow and to minimise the turbulence level. The spanwise width of the wind tunnel L_z was 170 mm, and the cross-stream diameter D_j of the jet was 21 mm; these values yielded the jet aspect ratio AR_j of 8.1. The length L_j of the jet inlet was 500 mm yielding the ratio $L_j/D_j = 23.8$, which is closed to that ratio of 20 in Jacob et al.

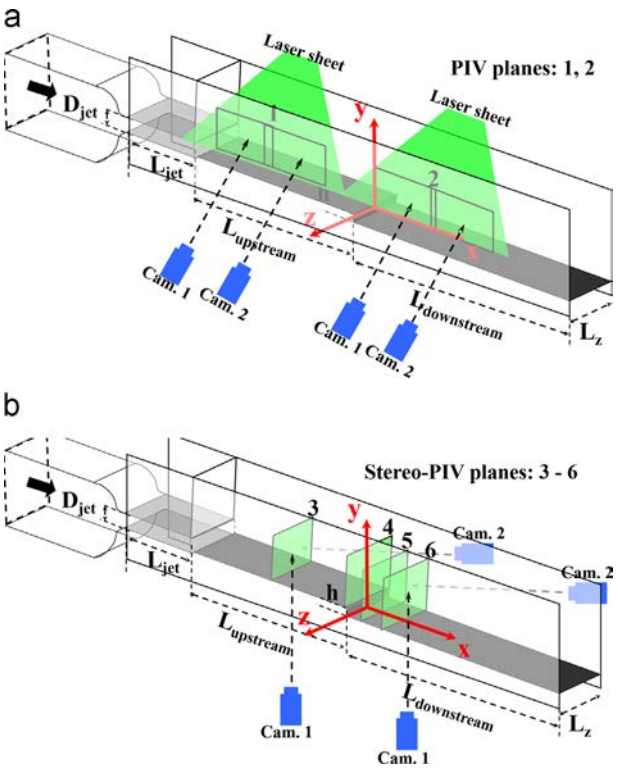

Fig. 2. Experimental configurations and PIV experimental setup of a turbulent plane wall jet over a backward-facing step: (a) PIV measurements along the central plane and (b) stereo-PIV measurements along the cross-stream planes.

[28], and sufficiently long for the flow to reach a fully developed state. Downstream of the jet nozzle, a plane wall jet was formed along a plate and was confined within two lateral walls to prevent flow spreading in the spanwise direction. The lateral walls were constructed of transparent plexiglass with a thickness of 10 mm to allow access for optical laser measurements.

The backward-facing step with the height $h = 15$ mm was located 500 mm downstream of the jet exit. Downstream of the step, the bottom wall was 450 mm long, i.e., 30 h, which was long enough to neglect the reverse flow effects far downstream. A hot wire anemometer, which was placed downstream of the jet nozzle, measured the jet exhaust velocity with an uncertainty of 1% of the mean flow. The mean jet velocity U_j was 17.35 m/s, and the jet Reynolds number Re_j, which was based on the flow speed, the jet cross-stream diameter D_j, and the kinematics viscosity ν, was 22,500. An olive oil droplet generator (TSI 9307) generated particles that had a mean diameter of 1 μm to seed the inlet of the centrifugal blower. The x, y and z coordinates, respectively, represent the horizontal, vertical and spanwise directions. The origin of the coordinate system is at the bottom step edge at the middle plane. The velocity components that correspond to the x, y and z directions are U, V and W for the time-averaged velocity and u', v' and w' for the fluctuating velocity, respectively.

2.1. PIV experimental setup

Fig. 2 shows the PIV experiment setup that consists of a two-dimensional two-component (2D2C) PIV system and a (2D3C) stereoscopic PIV system. The flow characteristics in the middle plane (xy) and at a region downstream of the jet exit, i.e., region 1, and at a region downstream of the backward-facing step, i.e., region 2, were investigated using the PIV system. The stereo-PIV system was used to measure all three velocity components in the wall normalspanwise (yz) planes at several streamwise positions. The cross-stream plane 3 was located at $x/h = -19.3$, i.e., $10D_j$ downstream of the jet exit, while the planes 4–6 were at the streamwise locations of $x/h = 0$, 2 and 4, respectively.

The PIV system was composed of a New Wave Nd:YAG laser (TSI Inc.) with an articulated light arm, two digital charge couple device (CCD) cameras, a synchroniser and a computer. The Nikkor camera lens had a 50-mm focal length and an f/5.6 aperture. Each laser beam of the double-pulsed laser was capable of 200 mJ/pulse at a wavelength of 532 nm. These beams were adjusted by a cylindrical lens and a spherical lens to form a 1-mm-thick laser sheet for the PIV measurements and a 2-mm-thick laser sheet for the stereo-PIV measurements. In the current experiments, the jet flow had a high mean streamwise velocity of $U_j = 17.35$ m/s. This value was the out-of-plane velocity component in the stereo-PIV measurements and possessed a three-dimensional structures due to the interactions with the lateral walls. The time interval between the first and second exposures should be small enough to minimise the out-of-plane particle displacements in the cross-plane stereo-PIV measurements. Adrian [2] suggested that the out-of-plane particle displacement between image pairs should not exceed one quarter of the laser thickness. To choose an appropriate thickness of the laser sheet and the time interval between the recordings, the authors have employed estimation methods suggested by Raffel et al. [51] and compromised with the above condition while maintaining reasonable mean particle displacements, i.e., a considerable signal-to-noise ratio in the cross-correlation calculations. The TSI PowerView Plus 4MP cameras with a resolution of 2048×2048 pixels and a pixel size of $7.4 \times 7.4\ \mu m^2$ captured PIV images and sent them directly to the computer. A LaserPulse (TSI Model 610035) synchroniser controlled the synchronization between the lasers and cameras. The time interval between the recordings for the stereo-PIV measurements varied from 20 to 30 μs, while the time interval for the PIV

measurements varied from 40 to 50 μs, yielding maximum particle displacements of 7 pixels.

In the PIV experiments, images of the fluid regions in the x–y planes with x/h ranging from -33.3 to -18.4 for region 1 and x/h ranging from -3.1 to 14.2 for region 2 were taken. At each of the regions (1 and 2), two cameras simultaneously captured the experimental images, and their fields of views were adjoined to spatially enlarge the fields of measurement. The streamwise overlapping zones of these cameras were 22 mm and 13 mm for region 1 and 2, respectively. A sequence of 1000 image pairs was recorded during each run, with a sampling rate of 1 Hz. The corresponding sampling interval, denoted by Δt, was 1 s. For region 1 (near the jet nozzle), non-dimensionalised by the mean jet velocity U_j and by the jet diameter D_j, this interval becomes $\Delta t \times U_j/D_j = 826$. For region 2 (downstream of the step), the sampling interval can be non-dimensionalised by the maximal streamwise velocity U_m measured at $x/h = 0$ (U_m was less than two-thirds of the jet velocity U_j, see Section 4.3) and the step height h, which is the largest-scale structure of the step flows. The corresponding interval is $\Delta t \times U_{max}/h = 771$. In all cases, the non-dimensionalised sampling interval shows that the particles travel a very long distance compared to the largest-scale structures of the flow. Therefore, the velocity fields that were obtained from the PIV image pairs are statistically independent.

In the stereo-PIV measurements, cameras viewed the y–z planes at angles of 45° from the streamwise x direction and on either side of the wind tunnel. The camera bodies were slightly rotated to satisfy the Scheimpflug condition for focusing in the laser sheet. The stereo-PIV measurements required the use of a calibration target to properly map the object plane, which was identified by the laser plane and the image plane, as defined by the camera sensor plane. The calibration target had two planes alternating in different depths (0.5 mm apart) and consisted of white markers that had a spacing of 2 mm in both the horizontal and vertical directions. Images of the target were captured by the stereo-PIV cameras and were processed to generate a mapping function between 2D image planes and a 3D object plane using the procedure of Soloff et al. [55]. A sequence of 2000 image pairs was taken at each streamwise location at the sampling rate of 1 Hz. As discussed in the previous paragraph, at this sampling rate, the three-component velocity fields obtained were statistically independent.

Image acquisition and image processing were performed with TSI Insight TM 4G software. The experimental image pairs were interrogated using a recursive Nyquist rectangular grid algorithm with multiple iterations and a 50% window overlap. The PIV images were processed with three iterations, of which the first-pass started with an interrogation window of 64×64 pixels while the final pass ended with an interrogation of 16×16 pixels. In the stereo-PIV image processing, two iterations were performed in which the square interrogation windows were 64×64 pixels and 32×32 pixels for the first and second iterations, respectively. Statistical validations were performed between iterations, including the final interrogation to identify and replace erroneous vectors. Vectors were computed from the correlation map with a Gaussian peak fit [51] for sub-pixel accuracy and were validated by a signal-to-noise ratio of 1.5. A median filter [62] was applied, and a standard deviation filter was used to remove spurious vectors. The erroneous vectors were then replaced by interpolation. In the stereo-PIV processing, pairs of two-dimensional displacement fields calculated from stereo-PIV images were reconstructed using the mapping function to obtain three-component velocity fields on the measurement plane. The grid-spacing in the PIV velocity vectors varied from 0.62 mm to 0.63 mm, i.e., from 0.041 h to 0.042 h, in the wall-normal and streamwise directions. In the stereo-PIV velocity vectors measured at different streamwise locations, the grid-spacing ranged from 1.23 mm to 1.57 mm, i.e., from 0.082 h to 0.105 h, in the wall-normal and spanwise directions. No low-pass filter was applied to the PIV and stereo-PIV velocity vectors.

For all the PIV and stereo-PIV measurements, the percentage of bad vectors calculated by the average over the number of velocity fields was approximately 2%. The uncertainties in the velocity measurements were estimated to be less than 4% of the mean jet velocity U_j. In the current experiments, uncertainty in velocity measurements can arise from two main sources. The first uncertainty was due to the Gaussian peak fit in the cross-correlation calculations that produced an uncertainty of 0.1 pixels, i.e. $0.04U_j$. The second uncertainty was a residual error by the least-square curve-fit when solving the four pixel-displacement equations in three unknowns [24,36]. The first uncertainty is usually dominant except when there is a flow field that has a high seeding concentration gradient, which was not observed in the current experiments. Dynamic range of the PIV measurements was approximated to 160 by following the estimations of Westerweel et al. [63] and Scarano and Riethmuller [52] where the displacement uncertainty of 0.1 pixels was applied.

3. Numerical simulations

To support a comparison with the PIV measurements, the experimental setup of the turbulent wall jet over the backward facing step shown in Fig. 2 was numerically produced with the same geometrical dimensions except for the conditioning section, to reduce the required computational cost. Fig. 3 shows the 20.2-million-point mesh of the 3D simulation domain, which was generated using the software GAMBIT based on block-structured grids. The computational domain extended from $10D_j$ upstream of the jet nozzle to $23.8D_j$ downstream of the jet exit and 30 h downstream of the backward-facing step. In the current experiment,

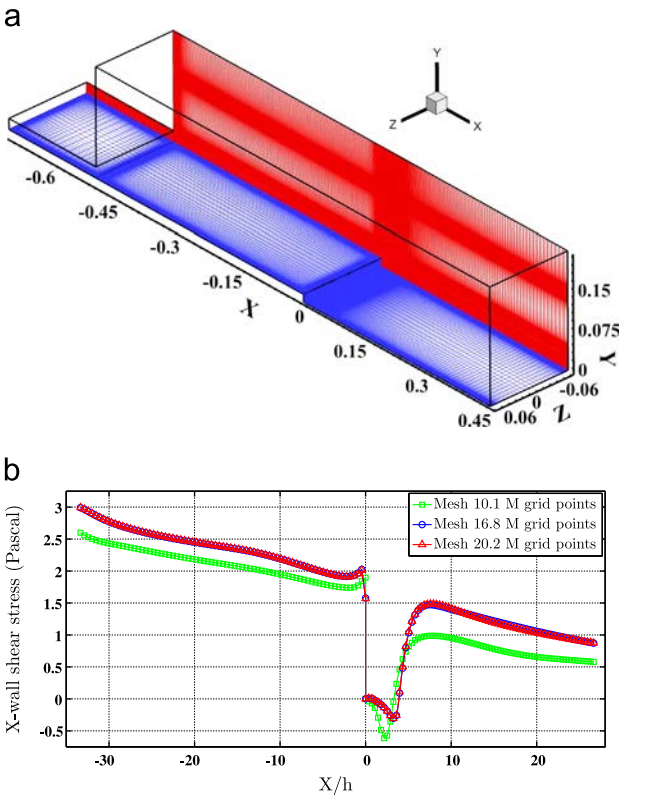

Fig. 3. Numerical simulation corresponding to the experimental setup in Fig. 2: (a) computational domain and the grid on a z-slice located at the vertical wall and (b) X-wall shear stress obtained from RANS simulations on different grids.

although the step AR was greater than 10, the upstream flow was a turbulent wall jet with the jet aspect ratio AR_j less than 10; three-dimensional effects from the side walls to the turbulent wall jet and turbulent backward-facing step were expected. The spanwise width of the simulation domain was similarly chosen to be that of the experimental setup, i.e., 170 mm. The wall-normal direction had a height of 225 mm ($10D_{j+h}$ or 15 h), which simulated the vertical walls and was high enough to ensure that the pressure effects do not overwhelm the turbulence effects [64,22].

Fig. 3(a) shows the structure of the generated mesh, where there are 592 points in the streamwise direction, 283 points upstream of the step and 348 points downstream of the step in the vertical direction and 120 points in the spanwise direction. In the region of the jet inlet and jet nozzle, the grid was compressed near the top wall, the bottom wall and the jet nozzle, where the stretching ratios between the heights of the inner grids to the adjacent grids were set to 1.13 and 1.19, respectively. In the region near the step, the grid was also compressed near the step edge and the step bottom wall with the stretching ratios of 1.025 and 1.17, respectively. In the spanwise direction, the grid was also fine enough toward the side walls with the stretching ratio of 1.12. The grid had a sufficiently high resolution close to the jet wall, the step wall and the vertical walls, and it was capable of resolving most of the developed boundary layers. To test the grid sensitivity, steady-state RANS simulations were performed on several grids. Fig. 3(b) shows a comparison of X-wall shear stress calculated by three grids of 10.1, 16.8 and 20.2 million grid points. The calculated wall shear stresses from the two finer meshes converged well. All the results presented in this paper are computed from the finest mesh, which was refined in all directions, but mostly near the rigid wall surfaces. For all the wall surfaces, the ranges of the non-dimensional wall-normal distance $y^+ < 1$. An inlet boundary condition was applied on the jet inlet surface of the simulation domain with a uniform velocity profile and turbulence intensity $I = 4\%$, which was equivalent to the turbulence intensity obtained from the experiments. On the top and at the back of the computational domain, a pressure outlet boundary condition was set to a relative pressure of 0 Pa. On the bottom and opposite walls of the current simulation domain, a non-slip boundary condition was imposed.

3.1. Numerical details on RANS simulations

The RANS simulation was performed by using the commercial fluid dynamics package FLUENT 6.3, in which the elliptic partial differential equations were solved by the finite-volume method. Turbulence calculations were performed using a second-order closure Reynolds stress model (RSM), which is the most elaborate turbulence model in FLUENT. The RSM does not apply the eddy-viscosity approach but directly solves transport equations for the Reynolds stresses and an equation for the dissipation rate. The exact Reynolds stress transport equation accounts for the directional effects of the Reynolds stress fields. The quadratic pressure-strain RSM introduced by Speziale et al. [57] with the default under-relaxation constants was used, and a standard first-order upwind discretization scheme was applied for the momentum, velocity, turbulent kinetic energy, turbulent dissipation rate and Reynolds stresses. This model has been proven to yield superior results for curved flows, re-circulating flows and basic shear flows including plane strain and axis-symmetric expansion and contraction. The flow configuration of the present study had flow expansions, shear layer separations at the jet nozzle and the leading edge of the step, a recirculation region downstream of the step and recirculation bubbles near the side wall; thus, the RSM was appropriately considered.

In the RANS calculation, the pressure-based solver, the implicit formulation and the Green–Gauss cell-based for the gradient option were chosen. The SIMPLE algorithm [48] was applied for the coupled pressure–velocity procedure. A non-equilibrium wall function [30] was applied for the near-wall treatment. An important advantage of this wall-treatment is that it employs the two-layer concept in computing the budget of turbulent kinetic energy for cells adjacent to walls. These cells are needed to solve the k equation at wall-neighboring cells that are assumed to consist of a viscous sub-layer and a fully turbulent layer. The RSM creates a high degree of coupling between the momentum equations and the turbulent stresses, it is then subjected to stability and convergence difficulties and expensive computational cost when compared to other turbulence models. The RSM calculation was initiated with a steady-state solution that was obtained from the 3D RANS simulation using a standard $k-\epsilon$ model to decrease the computation time and aid in the calculation convergence. Iterative calculations were further executed until the maximal residuals of the continuity, velocity, k, ϵ and Reynolds stresses converged to less than 10^{-5}. The RSM simulation was performed using four nodes on the FORTUNE cluster at the UVHC supercomputing centre. The CPU calculation time was approximately 72 s for 1 iteration, and the total iterations were 73,000.

4. Results and discussion

This section presents the flow field results obtained from the PIV measurements and the RANS simulation, where experimental and numerical flow statistics calculated from the central plane of the jet inlet region are validated first to ensure that the turbulent flow is fully developed prior to the nozzle. Next, mean flow fields

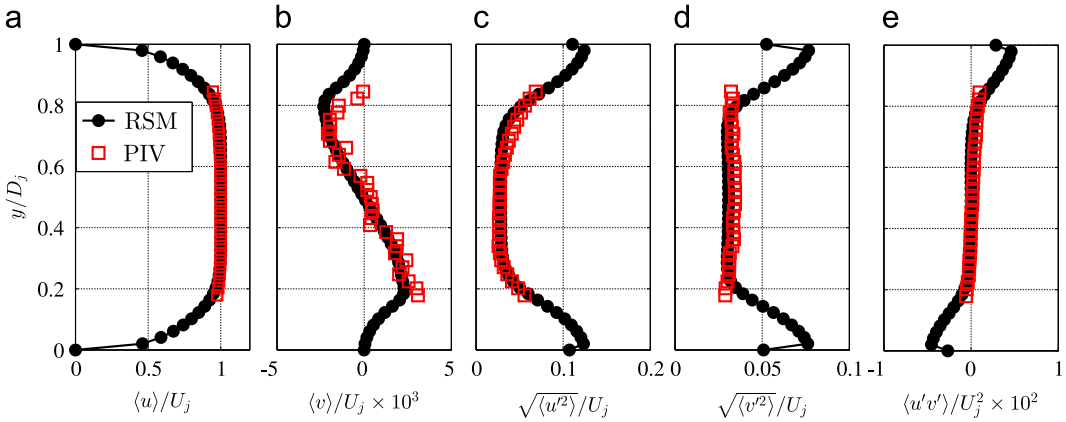

Fig. 4. Comparison of $\langle u\rangle/U_j$ and vertical $\langle v\rangle/U_j$ velocities and Reynolds stresses $\sqrt{\langle u'^2\rangle}/U_j$, $\sqrt{\langle v'^2\rangle}/U_j$ and $\langle u'v'\rangle/U_j^2$ at $(x+L_{upstream})/D_j = -4$ obtained by the PIV measurement and the RSM simulation.

and second-order statistical moments computed from the wall jet region (planes 1 and 3) and the backward-facing step region (planes 2, 4, 5 and 6) are presented.

4.1. Inlet flow

The inlet flow was measured in the central, vertical plane of the jet inlet region with the same 2D PIV setup as previously described to examine the flow development prior to the jet exit. Due to disturbances from Plexiglas acrylic glue close to the wall, reliable velocity measurements could not be performed within a gap of $0.14D_j$ from the top and bottom walls. Fig. 4 shows the non-dimensional mean velocities and turbulence intensities at the streamwise location $(x+L_{upstream})/D_j = -4$ obtained by the PIV measurement and RSM simulation. The PIV mean streamwise velocity, $\langle u\rangle/U_j$, profiles agree well to those of the RSM simulation. Note that in the bulk flow region, i.e. $y/D_j = 0.2$–0.8, the $\langle u\rangle$ component is strongly dominant, with a maximal two-order magnitude higher than the $\langle v\rangle$ component, and the comparison shown in Fig. 4(b) is satisfied. The Reynolds stresses $\sqrt{\langle u'^2\rangle}/U_j$, $\sqrt{\langle v'^2\rangle}/U_j$ and $\langle u'v'\rangle/U_j^2$ from the PIV measurements follow those from the RSM simulation rather well. The effect of erroneous velocity vectors caused by the disturbances from Plexiglass glue on the wall has yielded a slightly asymmetry of the $\sqrt{\langle u'^2\rangle}/U_j$ profile starting from the vertical location of $y/D_j = 0.7$. The results from the RANS simulation show turbulence peaks of 12% near the walls where the turbulent boundary layers are developed. In the middle of the channel, a lower turbulence level was experimentally observed and was correctly predicted by the RSM simulation.

4.2. Wall jet flow

In this section, results from the PIV measurement along the central x–y plane and cross-plane stereo-PIV measurements along the streamwise locations $x/h = -19.3$ (about $10D_j$ downstream of the jet exit), i.e. planes 1 and 3 in Fig. 2 respectively, are presented. First, parameters that govern the characteristics of the wall jet flow are noted. The inner region is determined by a region that extends from the wall up to a vertical point that is located at the wall distance y_{max}, where the mean velocity U_m reaches its maximal value $U_{max} = U(y_{max})$. The outer region is considered to be beyond y_{max}, i.e., $y > y_{max}$. The wall jet half-width $y_{1/2}$ is defined as the distance from the vertical point where $U(y_{1/2}) = 0.5U_{max}$ towards the wall. The inner region is generally similar to a boundary layer, while the outer region away from the maximum is similar to a free shear layer [59].

Fig. 5(a and b) shows the non-dimensionalised mean velocity vectors and non-dimensionalised turbulent kinetic energy obtained by the PIV measurement. It can be observed from the color contour that the maximum velocity decreases in the downstream direction while the thickness of the wall jet grows rapidly. The study of Eriksson et al. [21] indicated that properties of the wall jet flow of $Re = 9600$ show insignificant difference between $x/D_j = 20$ and 40. Their results suggested that the flow is in transitional state in the region $x/D_j < 10$, very close to being self-similar at $x/D_j = 20$, and reaches its full self-similarity far downstream around $x/D_j = 70$ [15]. Fig. 6(*left*) compares PIV profiles of $\langle u\rangle/U_j$ and $\sqrt{\langle u'^2\rangle}/U_j$ at $x/h = -2$, -1 and 0, i.e. $x/D_j > 20$ downstream of the jet outlet, and also illustrates that the plane wall jet flow is rather close to self-similarity state at the step edge. In the current configuration, the wall jet flow of $Re = 24,100$ was measured within the region of $10D_j$ downstream of the jet nozzle, where the flow is in transitional state.

Velocity streamlines illustrated in Fig. 5(c and d) show a qualitatively good agreement between the PIV and RSM results in the jet flow region. However, the PIV streamlines display an upward flow near the vertical wall on the top of the jet nozzle and this could be due to a recirculation in the surrounding medium. Fig. 5(e) shows a contour of the normalized vorticity calculated from the instantaneous PIV velocity. In the current configuration, the turbulent boundary layer is formed in the inlet channel. Due to a sudden expansion on the top wall, a shear layer is created from the jet nozzle and travels further downstream after rolling up into vortices. Inside this shear layer, the maximal turbulence level reaches almost 20% of the mean jet velocity U_j at the streamwise location $10D_j$ downstream of the nozzle, as seen in Fig. 6*(right)*. In addition, the turbulence level reduces slowly and remains fairly high when it reaches the edge of the step (see Section 4.3). A good agreement is observed in the maximum turbulent intensity calculated from the PIV measurement and RSM simulation in the region near the jet outlet. In Jacob et al. [28], the maximal turbulence level of approximately 22% of the mean jet velocity U_j in the jet mixing layer was found at $7D_j$ downstream of the jet nozzle. On the other hand, the turbulent boundary layer on the bottom wall channel continuously develops similar to a layer on a rigid flat plate. Head and Bandyopadhyay [25] and Tsai et al. [59] have discussed that the flow structure near the bottom wall consists of many irregular flow patterns, such as large bulges and hairpin vortices. In our experiments, it can be seen that large flow patterns, which grow in the downstream direction, are transported into the outer region by the vertical velocity fluctuations. Fig. 5(e) illustrates the interaction between the near wall structures and the shear layer eddies starting from $6D_j$ downstream and in the intermediate zone of the inner and outer regions.

Fig. 7 shows the normalized $\langle u\rangle/U_j$, $\langle v\rangle/U_j$, $\langle w\rangle/U_j$ velocities and the Reynolds stresses $\sqrt{\langle u'^2\rangle}/U_j$, $\langle u'v'\rangle/U_j^2$ and $\langle u'w'\rangle/U_j^2$ obtained at $x/h = -19.3$, i.e., $10D_j$ downstream of the jet nozzle. LDA results from Eriksson et al. [21] and Nait Bouda et al. [37] at the streamwise location $x/h = -17$ were over-plotted for the comparisons. The agreement among the $\langle u\rangle/U_j$ and $\langle v\rangle/U_j$ velocities was good, and the maximal streamwise velocity was less than the outlet velocity U_j. The $\langle u\rangle/U_j$ and $\langle v\rangle/U_j$ velocities from Eriksson et al. [21] and Nait Bouda et al. [37] showed the flatter profiles starting from $y/Y_{1/2} > 0.5$. In the comparisons of $\sqrt{\langle u'^2\rangle}/U_j$ and $\langle u'v'\rangle/U_j^2$, the PIV results overlapped with the stereo-PIV measurements, but they were slightly under-estimated by the RSM calculation. In Fig. 7(e),the $\langle w\rangle$ velocity profile fluctuated with the maximal deviation by approximately 2% of the U_j velocity at the middle of the jet half-width $y_{1/2}$. The normalized $\langle u'w'\rangle/U_j^2$ stress was smaller by an order of magnitude compared to the profile of Nait Bouda et al. [37]. From the obtained results, the two-dimensionality of the flow downstream of the jet nozzle with the aspect ratio of 8.1 could not be confirmed. Further evidence of the three-dimensionality of the flow downstream of the backward-facing step is discussed in the next section.

4.3. Backward-facing step flow

This section presents the results from the PIV measurements along the central x–y plane and the cross-plane stereo-PIV measurements along the streamwise locations $x/h = 0$, 2 and 4. These planes correspond to planes 2, 4, 5 and 6 in Fig. 2.

Fig. 8(a and b) shows the non-dimensionalised mean velocity vectors and the non-dimensionalised turbulent kinetic energy obtained by the PIV measurements. The flow upstream of the step can be normally considered as an unperturbed plane wall jet. At the edge of the step, the maximal streamwise velocity $U_{max}(x/h = 0)$ was found to be less than 70% of the jet velocity U_j as also found in Jacob et al. [28]. The $U_{max}(x/h = 0)$ is used in this paper as a reference velocity U_m for the step flow. Downstream of the step, the flow is characterized by a recirculation region as observed in Fig. 8(a–d). From the jet nozzle, the turbulent plane wall jet evolves

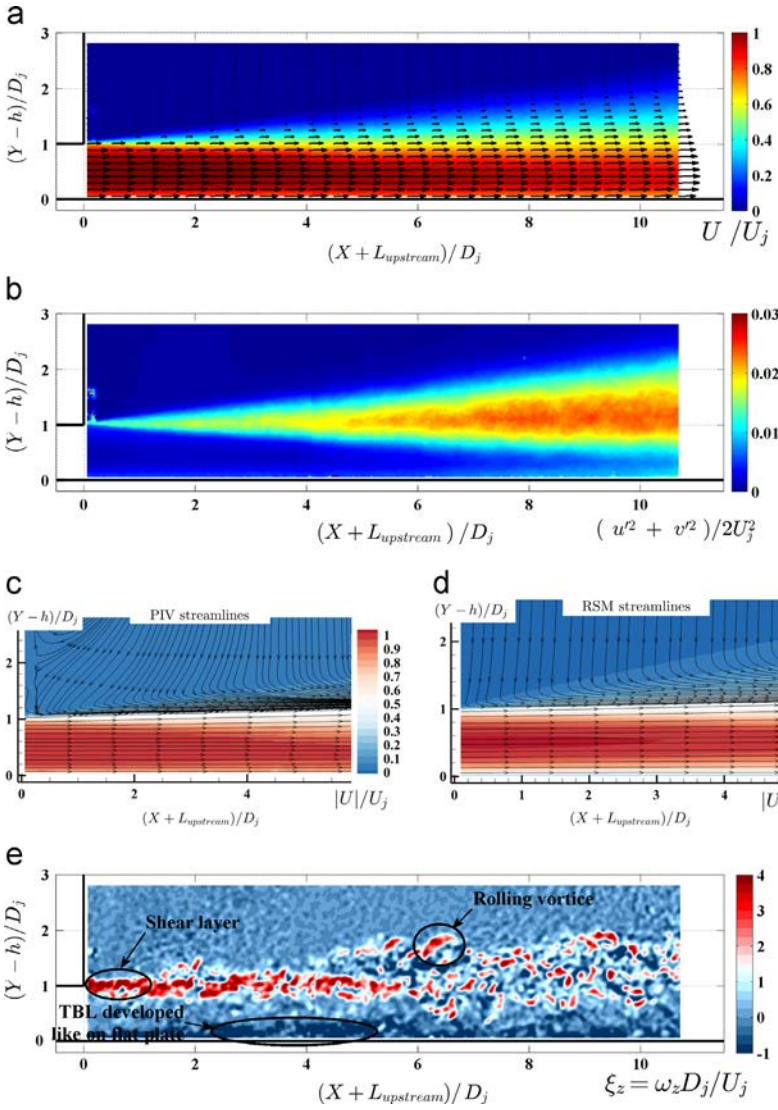

Fig. 5. Results obtained from the wall jet flow region (plane 1 in Fig. 2). Non-dimensionalised mean velocity vectors (a) and non-dimensionalised turbulent kinetic energy (b) obtained from the PIV measurement; the color shows the magnitude normalized by U_j and U_j^2, respectively. Velocity streamlines were calculated from the PIV measurement (c), and the RSM simulation (d). Instantaneous vorticity from the PIV measurement (e); the color shows the normalized vorticity magnitude, $\xi_z=\omega_z D_j/U_j$. (For interpretation of the references to color in this figure caption, the reader is referred to the web version of this paper.)

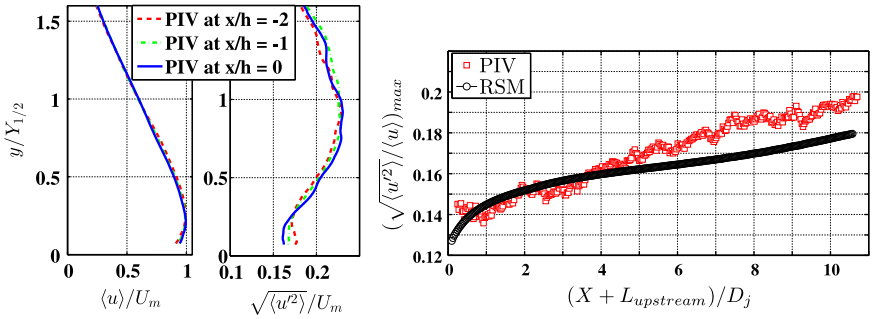

Fig. 6. $\langle u\rangle/U_j$ and $\sqrt{\langle u'^2\rangle}/U_j$ obtained by PIV measurement at $x/h=-2$, -1 and 0 *(left)* and streamwise distribution of the maximum turbulence intensity *(right)* from the PIV measurement and RSM simulation.

in the streamwise direction. At the step edge, the shear layer is created due to a sudden expansion in the vertical direction. A highly turbulent region is observed in the shear layer that is generated by the step and possesses a maximum turbulence level of 30% of the reference velocity U_m, i.e., approximately 20% of the jet velocity U_j (cf., Fig. 8(g)). Jacob et al. [28] found that the highest turbulent region was in the free shear layer that was generated by the step, with a maximum level of 39% of U_m or 23% of U_j, just upstream of the reattachment point.

Behind the step, the shear layer reattaches to the bottom wall at a time-averaged streamwise location X_r, which is a characteristic length of the backward-facing step flow. To measure X_r, the authors performed a near-wall measurement by using an Interfacial PIV technique [44]. The Interfacial PIV (IPIV) technique has been

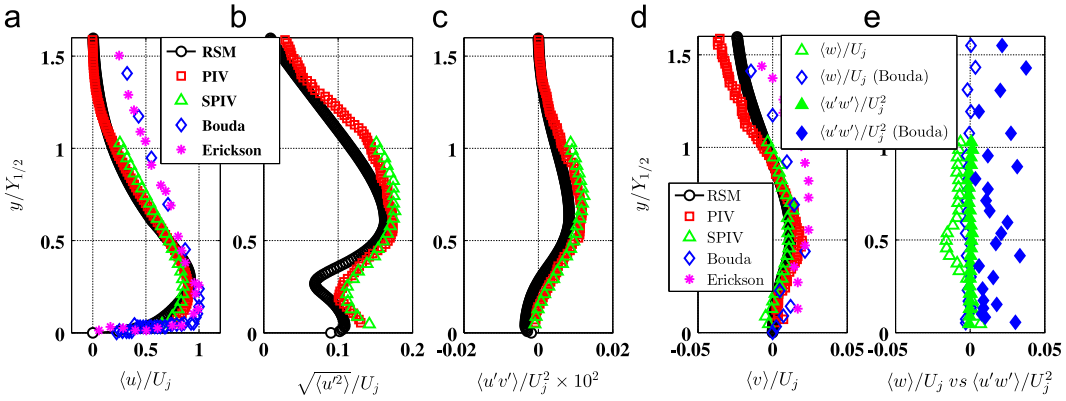

Fig. 7. Comparison of $\langle u\rangle/U_j$, $\langle v\rangle/U_j$ and $\langle w\rangle/U_j$ velocities, and Reynolds stresses $\sqrt{\langle u'^2\rangle}/U_j$, $\langle u'v'\rangle/U_j^2$ and $\langle u'w'\rangle/U_j^2$ at $x/h = -19.3$, i.e., $10D_j$ downstream of the jet nozzle, obtained by the PIV and stereo-PIV measurements and RSM simulation.

successfully applied to measure the wall shear stress [40] and near-wall velocity [42,39]. In the current experiments, the lengths X_r derived from the PIV experiment and RSM simulation were 3.55 h and 3.84 h, respectively, which are greater than those of $X_r = 2.75$–3 h obtained by Jacob et al. [28] and shorter than $X_r = 4.5$ h measured by Nait Bouda et al. [37]. Note that the experimental setups of the turbulent wall jet over the backward-facing step in Jacob et al. [28] and Nait Bouda et al. [37] were the most compatible with our test configuration, except for the differences in the Reynolds numbers and aspect ratios. The jet Reynolds number in Jacob et al. [28] was 10 times greater than that in our experiment, and the aspect ratios varied from 10 to 20. In Nait Bouda et al. [37], the step Reynolds number was three times smaller than that in our experiments, and the aspect ratio was 35. Unfortunately, the results presented in Jacob et al. [28] were available only for the case of an aspect ratio AR=20; a direct comparison between their results of AR=10 and our results could not be made. The X_r lengths from our test configuration were shorter than those varied from $X_r = 4.8$ h to 6.28 h measured in the backward-facing step flows with the top fixed wall [35,31,53,50]. Several authors have discussed many parameters, such as the Reynolds number, inlet turbulent intensity, aspect ratio, and expansion ratio, which yield the differences between X_r obtained from numerical simulations and experiments. Durst and Tropea [19] and Chang and Seung [12] have shown that an increase in the expansion ratio delayed the reattachment downstream of the step due to an adverse pressure gradient. Kuehn [32] showed that the recirculation length was increased when the expansion ratio was increased. Our test configuration did not possess a top fixed wall and could be considered to be an infinite expansion ratio, but that approach has not yielded a greater circulation length [3]. It can be argued that in addition to the differences in the upper boundary condition, the differences in the upstream flow, i.e., the turbulent plane wall jet in our test configuration, and the turbulent channel flow in the experiments and simulations of Jovic and Driver [29], Le et al. [35], Kostas et al. [31], Piirto et al. [50], primarily cause the short recirculation length in our configuration. Indeed, Isomoto and Honami [27] have observed that the higher turbulence levels of the incoming flows possibly had a shortening effect on the reattachment length. In our experiments, the turbulence intensity of the incoming wall jet reaches approximately 24% of the reference velocity U_m. This level was higher than that of the duct flow in the studies of Stevenson et al. [58], Vogel and Eaton [61] and Ötügen [46] and strongly enhances the cross-stream diffusion momentum [28]. Finally, it is necessary to note that the turbulent wall jet over a backward-facing step in this study is characterized by three length-scales, i.e., the vertical height y_m of the inner region, the jet half width $Y_{1/2}$ for the wall jet flow, and the step height h for the backward-facing step flow. The height y_m of the inner region measures the wall bounded viscosity against the jet momentum. The jet half-width $Y_{1/2}$ characterises the inertia of the wall jet flow, with which a small value of $Y_{1/2}$ facilitates the bending of the shear layer toward the bottom wall [28]. Note that if the wall jet reaches its full self-similarity state when approaching the step edge (not clearly observed in this study), y_m and $Y_{1/2}$ are no longer independent. In comparison between the backward-facing step with a wall jet upstream and the backward-facing step in a duct flow, the jet half-width $Y_{1/2}$ is typically smaller than the duct diameter, and both values represent the streamwise momentum. Therefore, the measured reattachment length X_r is shorter than that from a backward-facing step in a duct flow.

In Fig. 8(c and d), the averaged streamlines show two recirculation bubbles behind the step. The secondary recirculation bubble has a counter-clockwise direction and extends approximately h and 0.75 h in the streamwise and vertical directions, respectively. The size of the secondary bubble is comparable to those experimentally found in Schram et al. [53] and Nait Bouda et al. [37]. The primary recirculation bubble has a clockwise direction and extends farther downstream toward the reattachment point. After striking to the bottom wall around the mean reattachment point, the flow slowly forms a plane wall jet. Fig. 8(e and f) shows two contours of vorticity calculated from two instantaneous PIV velocity fields. These plots reveal a well-known flapping motion of the backward-facing step flow that has been discussed in the experiments of Eaton and Johnston [20], Driver et al. [17], the LES of Friedrich and Arnal [23], and the DNS of Le et al. [35]. The shear layer originates from the step edge and fluctuates in the vertical direction, which causes the reattachment location to oscillate. The mechanism of vorticity generation by the shear layer at the step edge was discussed in Le et al. [35], where the authors have used their DNS to study the movement of the turbulent vortices by observing pressure fluctuations around the reattachment region.

Fig. 9 shows instantaneous velocity fields and corresponding vorticity contours obtained by the stereo-PIV measurements at $x/h = 0$ and 2. This figure illustrates a high population of streamwise vortices and a high degree of three-dimensionality of the flow. Neto et al. [38] and Le et al. [35] have observed the most turbulent activities near the reattachment, the strong longitudinal vortices near the separated zone, and a quiet flow above $y/h = 2$. Note that in the DNS of Le et al. [35], a no-stress wall boundary condition was applied to the upper wall, the flow was assumed to be statistically homogeneous and periodic boundary conditions were used in the spanwise direction. In addition, the inlet flow was taken from the turbulent boundary layer in the channel flow [56]. In contrast to the quiet flow observed in Neto et al. [38] and Le et al. [35], the instantaneous velocity vectors and vorticity contour in Fig. 9 show the very strong and large-scale

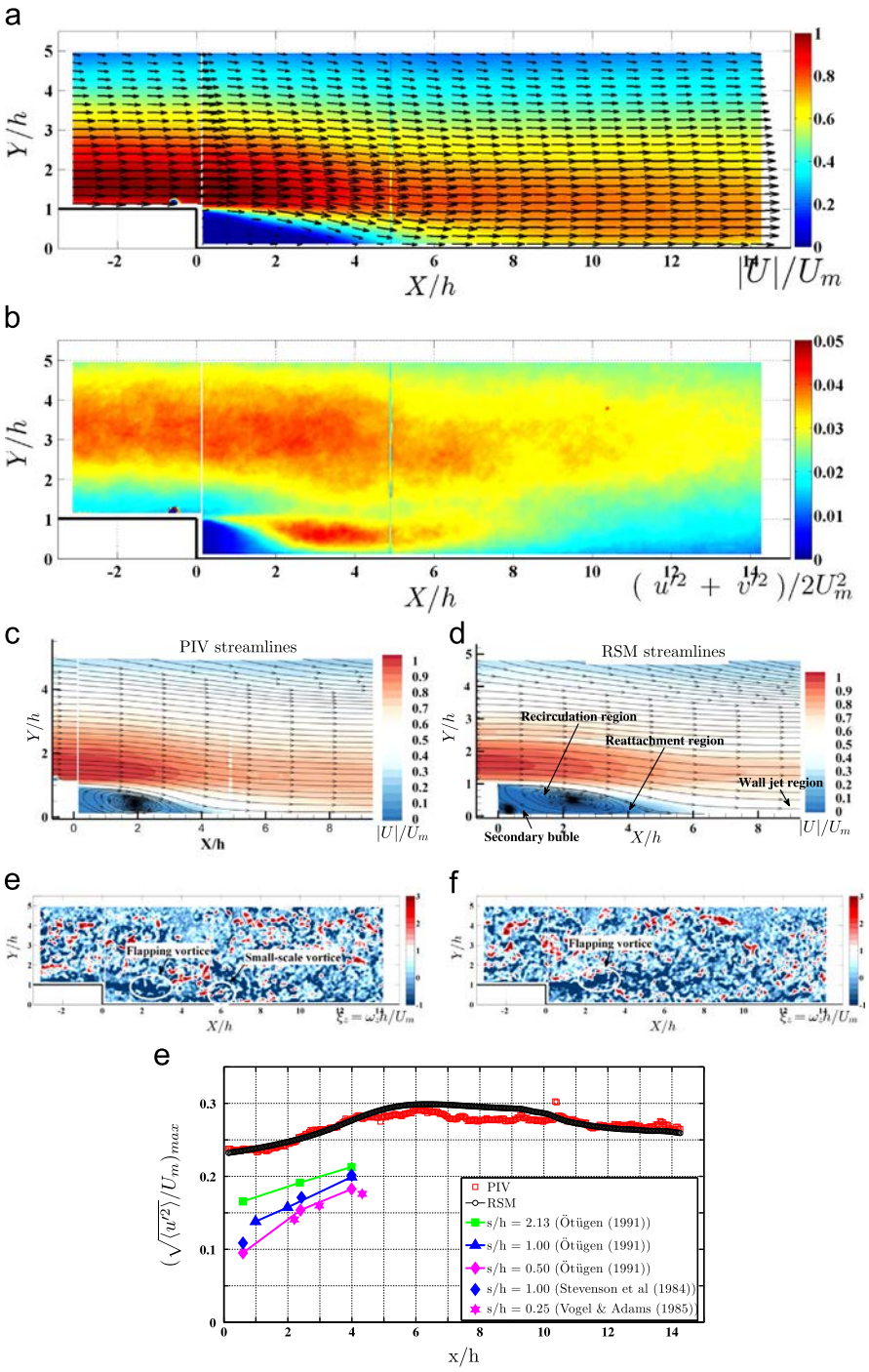

Fig. 8. Results obtained from the backward-facing step flow region (plane 2 in Fig. 2). Non-dimensionalised mean velocity vectors (a) and non-dimensionalised turbulent kinetic energy (b) obtained from the PIV measurement; the color shows the magnitude normalized by U_m and U_m^2. Velocity streamlines calculated from the PIV measurement (c), and the RSM simulation (d). Instantaneous vorticity from the PIV measurement (e and f); the color shows the normalized vorticity magnitude, $\xi_z = \omega_z h/U_m$. Streamwise distribution of the maximum turbulence intensity (g). (For interpretation of the references to color in this figure caption, the reader is referred to the web version of this paper.)

counter-rotating streamwise vortices in a region that ranges from $y/h = 2$ to $y/h = 5.3$. Additionally, these figures display streamwise vortices near the side walls and the corners formed by the side walls and the bottom wall. These structures have not been observed in previous studies of the two-dimensional backward-facing step. The vortices could originate from the interactions between the side walls and the shear layer of the plane wall jet upstream or the shear layer of the backward-facing step. The vorticity generation by the side walls and the shear layer upstream is illustrated by the instantaneous velocity vectors and vorticity contour from the stereo-PIV measurements at the streamwise location $x/h = 0$, which shows three streamwise vortices occurring near the right vertical wall.

The presence of the corner vortices was observed in a few three-dimensional backward-facing step studies [64,13,60,9]. Williams and Baker [64] reported the presence of the side walls result in the formation of a wall-jet, which is located at the bottom wall and points from the side walls toward the symmetry plane. Biswas et al. [9] discussed that the jet-like flow developing in the corner of the side wall and the bottom wall is the culmination of the

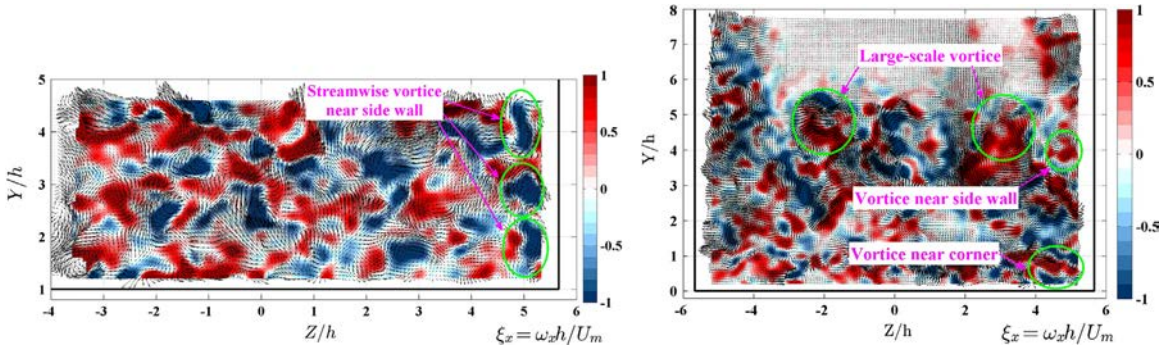

Fig. 9. Instantaneous streamwise vorticity obtained from the cross-plane stereo-PIV measurements at $x/h = 0$ and 2 (planes 4 and 5 in Fig. 2). Solid black lines display the bottom and vertical walls. Vectors are the in-plane velocity components, w and v. The color shows the normalized vorticity magnitude, $\xi_x = \omega_x h/U_m$. (For interpretation of the references to color in this figure caption, the reader is referred to the web version of this paper.)

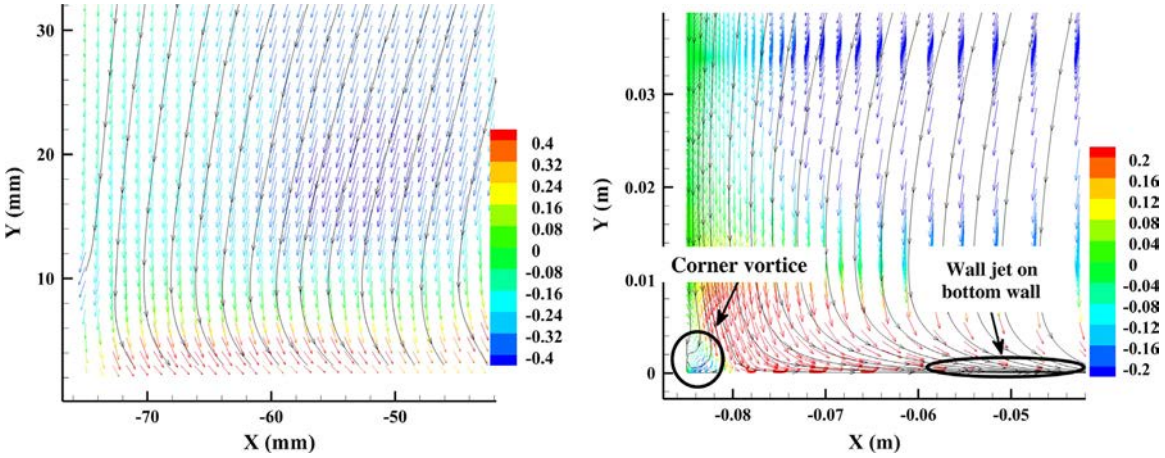

Fig. 10. In-plane velocity vectors, w and v components, and velocity streamlines from the cross-plane stereo-PIV measurements *(left)* and the RSM simulation *(right)* at the cross-stream plane $x/h = 4$ (plane 6 in Fig. 2). Color shows the spanwise velocity w. The RSM velocity vectors are de-sampled to aid the visualization. (For interpretation of the references to color in this figure caption, the reader is referred to the web version of this paper.)

generation of the spanwise velocity (the w component) from the side wall. The phenomena were also observed in the current experiments and RSM simulation. In Fig. 10, in-plane mean velocity fields ($\langle w \rangle$, $\langle v \rangle$) obtained at the cross-stream plane $x/h = 4$ illustrate the presence of the wall-jet formation on the bottom wall and the corner vortices. Near-wall velocity measurements for the stereo-PIV experiments could not be produced because of strong laser reflection on the vertical and bottom walls. However, the derived velocity streamlines confirmed the formation of the jet flow on the bottom wall and its direction toward the middle plane.

Fig. 11 compares the $\langle u \rangle / U_m$, spanwise $\langle w \rangle / U_m$ velocities and Reynolds stresses $\sqrt{\langle u'^2 \rangle}/U_m$, $\langle u'v' \rangle / U_m^2$ and $\langle u'w' \rangle / U_m^2$ obtained at $x/h = 0$. The agreement among the $\langle u \rangle / U_m$ profiles was good. These profiles also compared favorably with the LDA results of Jacob et al. [28]. The turbulence peaks of the PIV experiments were reproduced fairly well by the RSM calculation, excepting that the PIV measurements could not produce the negative peak of $\langle u'v' \rangle / U_m^2$ due to the limitation of PIV measurements at wall. The $\langle u'w' \rangle / U_m^2$ profile showed a weak turbulence production, and the normalized $\langle w \rangle / U_m$ velocity showed a velocity fluctuation of 2.5% of U_m. Similar to the observation in Fig. 7, this finding indicated that the inner part of the incoming jet flow deviated slightly to the vertical side wall.

Fig. 12 presents the evolution of the $\langle u \rangle / U_m$ velocity and Reynolds stresses $\sqrt{\langle u'^2 \rangle}/U_m$, $\sqrt{\langle v'^2 \rangle}/U_m$, $\langle u'v' \rangle / U_m^2$ and $\sqrt{\langle w'^2 \rangle}/U_m$ obtained at $x/h = 2$ and 4. A small discrepancy of the $\langle u \rangle / U_m$ profiles can be seen in the vicinity of the wall at $x/h = 4$. This streamwise section is located in an unsteady zone where the shear layer impinges on the bottom wall and generates smaller vortices. The shear layer impingement and vorticity generation possess complex, three-dimensional flow structures that produce particle displacements that are normal to the laser sheet, which affects the accuracy of the PIV measurements. In the region $y/h > 2$, the $\langle u \rangle / U_m$ velocity of Badri Kusuma [6] and Nait Bouda et al. [37] showed the flatter profiles.

In the comparisons of $\langle u'v' \rangle / U_m^2$, the RSM profiles were in good agreement with those from the PIV and stereo-PIV measurements. In the study of Fadai-Ghotbi et al. [22], the Unsteady RANS (URANS) of the BFS with $Re_h = 37,500$ using the Elliptic Blending Reynolds Stress Model (EB-RSM) estimated the reattachment length within a 5% error; the recirculation region was too thick, and the shear strain was too weak. As a result, the shear stress in the circulation region was under-estimated, and the recovery of the boundary layer downstream of the reattachment was not satisfactory. In the current study, the RSM simulation slightly over-estimated the reattachment length by approximately 8%; the streamwise velocity and the shear stress $\langle u'v' \rangle / U_m^2$ of the PIV and stereo-PIV measurements were satisfactorily predicted by the RSM simulation.

The $\sqrt{\langle u'^2 \rangle}/U_m$ profiles of the PIV measurements are predicted well by the RSM simulation in the region $y/h < 2$. In the region $y/h > 2$, the RSM simulation over-predicted by 15% the turbulence levels compared to the PIV and stereo-PIV experiments. The $\sqrt{\langle v'^2 \rangle}/U_m$ from the PIV and stereo-PIV measurements were fairly predicted by the RSM simulation with an approximate 10%

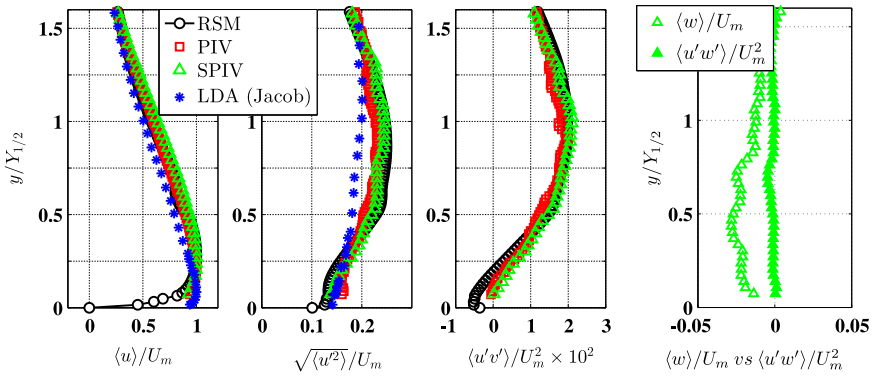

Fig. 11. Comparison of $\langle u\rangle/U_m$ and $\langle w\rangle/U_m$ velocities, and the Reynolds stresses $\sqrt{\langle u'^2\rangle}/U_m$, $\langle u'v'\rangle/U_m^2$ and $\langle u'w'\rangle/U_m^2$ at $x/h=0$ obtained by the PIV and stereo-PIV measurements and the RSM simulation.

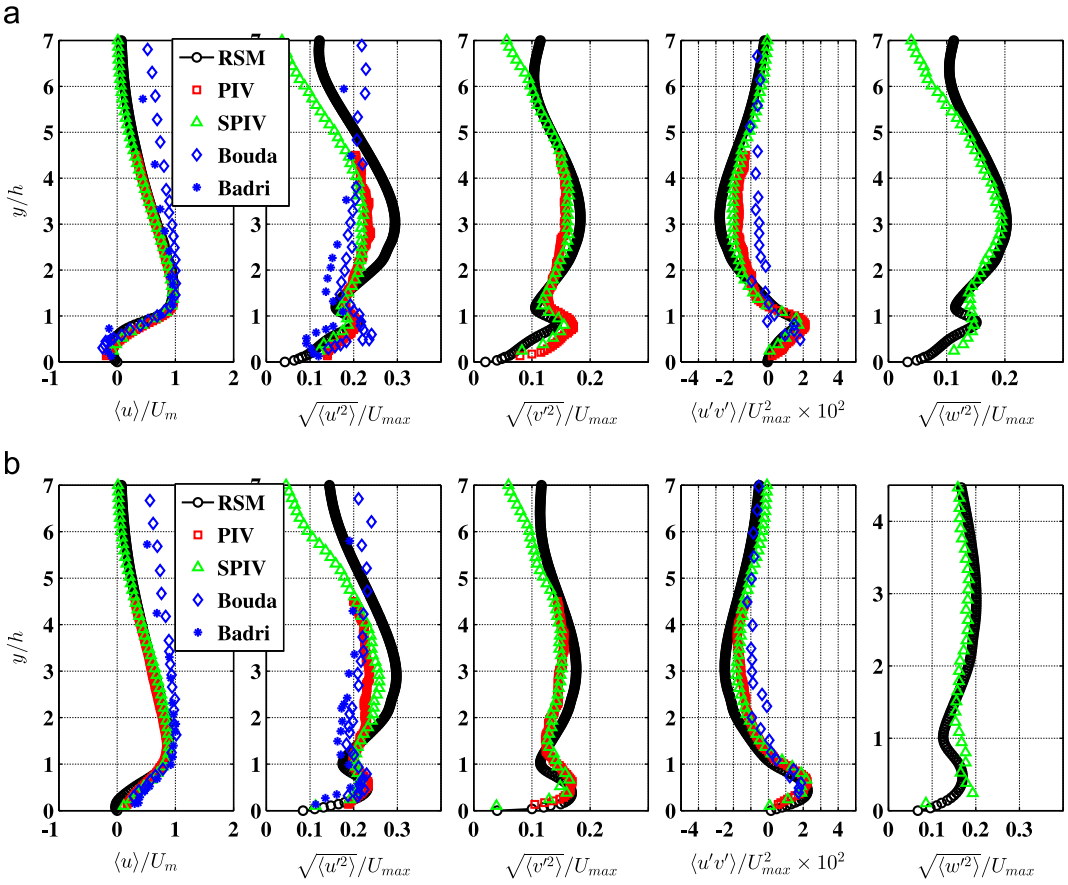

Fig. 12. Comparison of $\langle u\rangle/U_m$ velocity and Reynolds stresses $\sqrt{\langle u'^2\rangle}/U_m$, $\sqrt{\langle v'^2\rangle}/U_m$, $\sqrt{\langle w'^2\rangle}/U_m$, and $\langle u'v'\rangle/U_m^2$ at $x/h=2$ and 4, obtained by the PIV and stereo-PIV measurements and the RSM simulations. (a) Non-dimensional mean velocities and Reynolds stresses at $x/h=2$ and (b) non-dimensional mean velocities and Reynolds stresses at $x/h=4$.

over-estimation in the region $y/h>2$, while better agreement was observed in the vicinity of the wall ($y<h$). The turbulence profiles $\sqrt{\langle w'^2\rangle}/U_m$ from the RSM simulation were in a fairly good agreement with those from the stereo-PIV measurement. The agreements in the comparisons of the mean velocity and turbulence profiles in Figs. 11 and 12 are satisfactory in the outer region, i.e., $y>Y_{1/2}$ and $y/h>2$. In Fig. 12, the discrepancies mainly appear in the comparison of $\sqrt{\langle u'^2\rangle}/U_m$.

Here, the authors discuss some of the main reasons that caused the differences between the present PIV and the stereo-PIV measurements and the RSM simulation. The first reason is the limitation in the 2D2C PIV measurements, i.e., they cannot account for particle motions that are perpendicular to the laser plane, and the limitation in the 2D3C stereo-PIV measurements, i.e,. they are encountered by a large out-of-plane velocity component that influences the experimental accuracy of the stereo-PIV systems, as discussed in Hutchins et al. [26]. The accuracy of the PIV measurements was influenced in the shear layers of the jet nozzle and the step edge and near the step in the recirculation, where particle displacements in the spanwise direction were considerable. Similar to the study of Hutchins et al. [26], the accuracy of the stereo-PIV measurements in our study was primarily affected by the large streamwise longitudinal velocity and the residual error. The residual error is unique to the stereo-PIV calculation and is caused by the least-squares

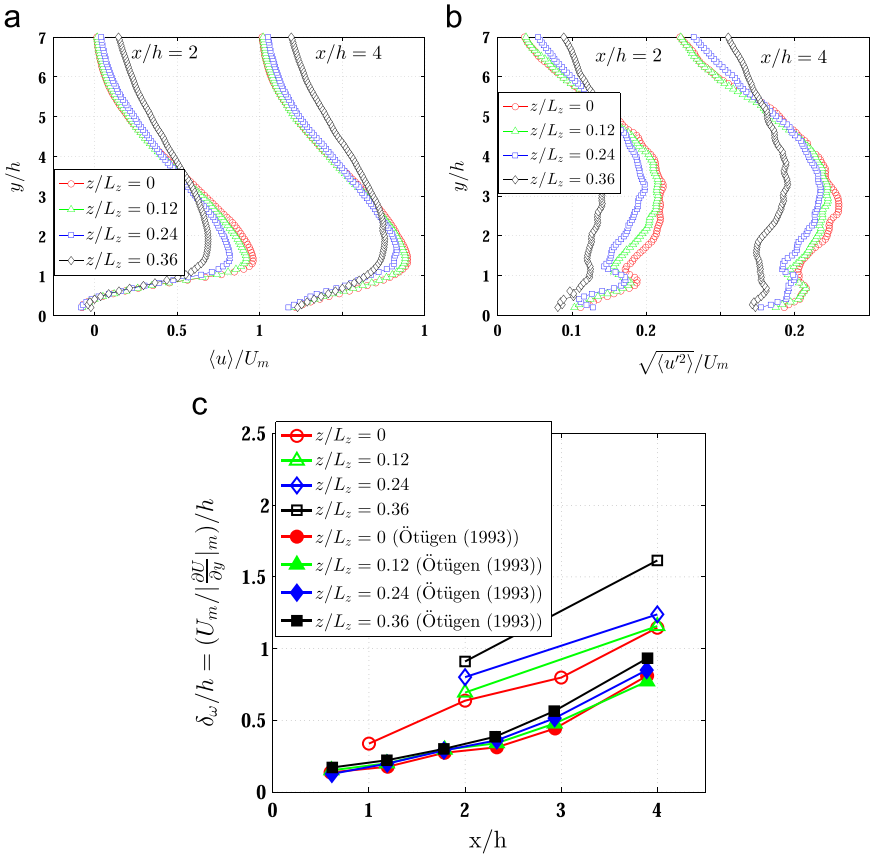

Fig. 13. $\langle u \rangle / U_m$ (a) and $\sqrt{\langle u'^2 \rangle}/U_m$ (b) at different streamwise and spanwise locations, and (c) shear layer vorticity thickness growth at different spanwise locations.

method that is used to solve four simultaneous pixel displacement equations to arrive at the three velocity components. Hutchins et al. [26] concluded that the residual error caused the uncertainties in the velocity measurements, which ranged from approximately $0.04U_m$ near the wall to $0.012U_m$ toward the free stream. Moreover, the mean particle displacements and the velocity dynamic range were limited due to a constraint from the laser thickness of 2 mm. Under these circumstances, the errors due to pixel locking were intensified especially in the near-wall region, where fluctuating displacements were less than 0.5 pixels and yielded the underestimations of the r.m.s velocity fluctuations and Reynolds shear stresses [14]. Second, the PIV and stereo-PIV measurements have the averaged-volume property [41], which is characterized by the laser thickness and the interrogation window size, i.e., approximately $1 \times 0.63 \times 0.63$ mm^3 and $2 \times 1.57 \times 1.57$ mm^3 for the PIV and stereo-PIV measurements, respectively. Although the RSM calculation under-predicted or over-predicted the PIV and stereo-PIV measurements at some locations, the overall agreement was satisfactory. In addition to the reasons discussed above, one should keep in mind that differences between the experimental conditions and the simulations are unavoidable [11,39]. For the turbulent wall jet flows and the backward-facing step flows, there are many important factors, such as the expansion ratio, the aspect ratio, the Reynolds number, the free stream turbulence, confined and unconfined channels, and other factors, which could influence the measurements. These factors solely or jointly yield the experimental results highly scattered and make the comparison between the experiments and simulations appear to be imperfect. Relevant remarks can be reviewed in Breuer [11] and Perrin et al. [49].

This paragraph discusses the three-dimensionality effects on the mean flow, where the spanwise uniformity is significantly distorted within a short streamwise distance from the step. Fig. 9 illustrates the primary mechanism for the three-dimensionality of the flow in the vicinity of the wall, where the streamwise vortex patterns are generated at the junction of the side walls and the step corner. The longitudinal vortices develop along the side walls, interact with the secondary flow pattern, and result in the rapid growth of the spanwise non-uniformity of the velocity with the axial distance [46]. Fig. 13(a and b) compares the $\langle u \rangle / U_m$ and $\sqrt{\langle u'^2 \rangle}/U_m$ profiles obtained at different streamwise positions, i.e., $x/h = 2$, 4 and 6, and various spanwise positions, i.e., $z/L_z = 0$, 0.12, 0.24 and 0.36. It is noticeable that at $x/h = 2$, the $\langle u \rangle / U_m$ and $\sqrt{\langle u'^2 \rangle}/U_m$ profiles obtained at $z/L_z = 0$ and 0.12 were in close agreement, while the profiles at $z/L_z = 0.24$ and 0.36 showed a significant deviation from the profiles at $z/L_z = 0$. These results indicated that there was a non-uniform shear layer thickness near the side walls and that the spanwise uniformity of the mean flow was limited to approximately a 50% depth of the channel. This observation was also found in Ötügen [46]. Indeed, Fig. 13 (c) shows the comparison of the separated shear layer vorticity thickness at various spanwise positions. The vorticity thickness is defined as

$$\delta_\omega = U_m / |\frac{\partial U}{\partial y}|_m, \tag{1}$$

where $|\partial U/\partial y|_m$ is the local maximum of the mean velocity gradient. Ötügen et al. [47] discussed that the shear layer grew non-linearly under the influence of the adverse pressure gradient and the streamline curvatures. It is observed that the shear layer vorticity thickness growth rates from Ötügen et al. [47] are at the same order of magnitude as those obtained our experiments but they remain smaller because of their lower starting value. We argue that the differences in the upstream flows, i.e., the plane turbulent channel and the confined top wall in Ötügen [46] and Ötügen et al. [47], yielded the discrepancy in the comparison. However, in both the results, the shear layer growth rates from

$z/L_z = 0.24$ increased with a larger spanwise distance from the middle channel, and the difference in the growth rate was greater downstream of the step. These results indicated that the two-dimensionality of the mean flow was distorted at a short distance downstream of the step from the spanwise location $z/L_z \geq 0.24$. It can now be confirmed that the existence of the streamwise vortices along the corners and the side walls strongly influences the mean velocity and the turbulence fields near the side walls.

5. Conclusions

In this paper, the flow characteristics of a turbulent wall jet over a backward-facing step in an unconfined wind tunnel with an aspect ratio of 8.1 were experimentally investigated by the PIV and stereo-PIV measurements. The jet Reynolds number was 24,100 and the step Reynolds number was 11,900. The velocity profiles and r.m.s fluctuating velocity distributions were obtained along the central plane and several cross-stream planes. The PIV results were compared with those obtained by the 3D RANS numerical simulation using a second-order closure Reynolds stress model (RSM). For the wall jet flow region, the experimental and numerical results showed that the turbulent boundary layer was formed in the inlet channel, and the shear layer was generated at the jet nozzle due to the sudden expansion. The shear layer had the maximal turbulence level of approximately 20% of the mean jet velocity U_j at the streamwise location $10D_j$ and was broken into vortices and travelled further downstream. For the backward-facing step flow, the PIV and stereo-PIV measurements illustrated that the maximal upstream velocity U_m was less than 70% of the jet velocity U_j. The turbulence intensity of the incoming jet flow reached approximately 24% of the velocity U_m, which was higher than that of the duct flow and strongly enhanced the cross-stream diffusion of momentum. The shear layer was generated at the step edge and possessed a high turbulence level, i.e., 30% of the velocity U_m. Compared to the backward-facing step flows with the plane channel upstream and the top fixed wall, the studied incoming flow had a higher turbulence level, which primarily caused the shorter recirculation length. The stereo-PIV measurements in the cross-stream planes revealed a high degree of three-dimensionality of the flow, which consisted of a high population of streamwise vortices in the upper region, near the side walls and the corners of the bottom wall and side walls. In addition, the obtained stereo-PIV results illustrated the formation of the jet-like flow on the bottom wall and its direction toward the middle plane. Finally, the obtained PIV and stereo-PIV measurements exhibited the three-dimensionality effects on the mean flow, where the streamwise vortices developed along the side walls and significantly distorted the spanwise uniformity of the mean flow within a short streamwise distance from the step.

Acknowledgments

The authors are grateful for the financial support provided by the MEDEE project, the French National Company of Electricity (EDF), the Région Nord Pas-de-Calais, and the European project FEDER.

References

[1] Adams E, Johnston J. Effects of the separating shear layer on the reattachment flow structure. Part 2: Reattachment length and wall shear stress. Exp Fluids 1988;6(7):493–9.
[2] Adrian RJ. Particle-imaging techniques for experimental fluid mechanics. Annu Rev Fluid Mech 1991;23(1):261–304.
[3] Aider JL, Danet A, Lesieur M. Large-eddy simulation applied to study the influence of upstream conditions on the time-dependant and averaged characteristics of a backward-facing step flow. J Turbul 2007(8):.
[4] Armaly B, Durst F, Pereira J, Schonung B. Experimental and theoretical investigation of backward-facing step flow. J Fluid Mech 1983;127(473):20.
[5] Arnal M, Friedrich R. Large-eddy simulation of a turbulent flow with separation. In: Turbulent shear flows, vol. 8; 1993. Springer, Berlin, Heidelberg. p 169–87.
[6] Badri Kusuma MS. Etude expérimentale d'un écoulement turbulent en aval d'une marche descendante: cas d'un jet pariétal et de la couche limite [PhD thesis]. Ecole Centrale de Nantes; 1993.
[7] Bhattacharjee P, Loth E. Simulations of laminar and transitional cold wall jets. Int J Heat Fluid Flow 2004;25(1):32–43.
[8] Bischof CH, Bücker HM, Rasch A. Sensitivity analysis of turbulence models using automatic differentiation. SIAM J Sci Comput 2004;26(2):510–22.
[9] Biswas G, Breuer M, Durst F. Backward-facing step flows for various expansion ratios at low and moderate Reynolds numbers. J Fluids Eng 2004;126:362–74.
[10] Bradshaw B, Gee M. Turbulent wall jets with and without an external stream; 1962. HM Stationery Office, London.
[11] Breuer M. A challenging test case for large eddy simulation: high Reynolds-number circular cylinder flow. Int J Heat Fluid Flow 2000;21(5):648–54.
[12] Chang PK, Seung RH. Effects of pressure gradient on reattaching flow downstream of a rearward-facing step. J Aircraft 1990;27(1):93–5.
[13] Chiang T, Sheu TW. A numerical revisit of backward-facing step flow problem. Phys Fluids 1999;11:862.
[14] Christensen K. The influence of peak-locking errors on turbulence statistics computed from PIV ensembles. Exp Fluids 2004;36(3):484–97.
[15] Dejoan A, Leschziner M. Large-eddy simulation of a plane turbulent wall jet. Phys Fluids 2005;17 025,102.
[16] Dejoan A, Wang C, Leschziner M. Assessment of turbulence models for predicting the interaction region in a wall jet by reference to LES solution and budgets. Flow Turbul Combust 2006;77(1-4):229–55.
[17] Driver D, Seegmiller H, Marvin J. Unsteady behavior of a reattaching shear layer. In: Sixteenth fluid and plasma dynamics conference, vol 1.; 1983.
[18] Driver DM, Seegmiller HL. Features of a reattaching turbulent shear layer in divergent channel flow. AIAA J 1985;23(2):163–71.
[19] Durst F, Tropea C. Turbulent, backward-facing step flows in two-dimensional ducts and channels. In: Proceedings of the third international symposium on turbulent shear flows; 1981. p. 1–18.
[20] Eaton JK, Johnston J. Turbulent flow reattachment: an experimental study of the flow and structure behind a backward-facing step; 1980. Stanford University.
[21] Eriksson J, Karlsson R, Persson J. An experimental study of a two-dimensional plane turbulent wall jet. Exp Fluids 1998;25(1):50–60.
[22] Fadai-Ghotbi A, Manceau R, Borée J. Revisiting URANS computations of the backward-facing step flow using second moment closures: influence of the numerics. Flow Turbul Combust 2008;81(3):395–414.
[23] Friedrich R, Arnal M. Analysing turbulent backward-facing step flow with the lowpass-filtered Navier–Stokes equations. J Wind Eng Ind Aerodyn 1990;35:101–28.
[24] Ganapathisubramani B, Longmire E, Marusic I. Investigation of three dimensionality in the near field of a round jet using stereo PIV. J Turbul 2002;3(016).
[25] Head M, Bandyopadhyay P. New aspects of turbulent boundary-layer structure. J Fluid Mech 1981;107:297–338.
[26] Hutchins N, Hambleton W, Marusic I. Inclined cross-stream stereo particle image velocimetry measurements in turbulent boundary layers. J Fluid Mech 2005;541:21–54.
[27] Isomoto K, Honami S. The effect of inlet turbulence intensity on the reattachment process over a backward-facing step. ASME Trans J Fluids Eng 1989;111:87–92.
[28] Jacob MC, Louisot A, Juvé D, Guerrand S. Experimental study of sound generated by backward-facing steps under wall jet. AIAA J 2001;39 (7):1254–60.
[29] Jovic S, Driver D. Backward-facing step measurement at low Reynolds number, Reh = 5000. NASA Technical Memorandum 108807; 1994.
[30] Kim SE, Choudhury D. A near-wall treatment using wall functions sensitized to pressure gradient. In: ASME FED, separated and complex flows; 1995.
[31] Kostas J, Soria J, Chong M. Particle image velocimetry measurements of a backward-facing step flow. Exp Fluids 2002;33(6):838–53.
[32] Kuehn DAD. Effects of adverse pressure gradient on the incompressible reattaching flow over a rearward-facing step. AIAA J 1980;18(3):343–4.
[33] Lancial N, Beaubert F, Harmand S, Rolland G. Effects of a turbulent wall jet on heat transfer over a non-confined backward-facing step. Int J Heat Fluid Flow 2013;44:336–47.
[34] Launder B, Rodi W. The turbulent wall jet measurements and modeling. Annu Rev Fluid Mech 1983;15(1):429–59.
[35] Le H, Moin P, Kim J. Direct numerical simulation of turbulent flow over a backward-facing step. J Fluid Mech 1997;330(1):349–74.
[36] Longmire E, Ganapathisubramani B, Marusic I, Urness T, Interrante V. Effective visualization of stereo PIV vector fields of a turbulent boundary layer. J Turbul 2003(23):4.
[37] Nait Bouda N, Schiestel R, Amielh M, Rey C, Benabid T. Experimental approach and numerical prediction of a turbulent wall jet over a backward facing step. Int J Heat Fluid Flow 2008;29(4):927–44.
[38] Neto AS, Grand D, Métais O, Lesieur M. A numerical investigation of the coherent vortices in turbulence behind a backward-facing step. J Fluid Mech 1993;256:1–25.
[39] Nguyen T, Harmand S. Heat transfer and vortical structures around a rotating cylinder with a spanwise disk and low-velocity crossflow. Int J Heat Mass Transf 2013;64:1014–30.

[40] Nguyen T, Wells J, Nguyen CV. Wall shear stress measurement of near-wall flow over inclined and curved boundaries by stereo interfacial particle image velocimetry. Int J Heat Fluid Flow 2010;31(3):442–9.
[41] Nguyen T, Pellé J, Harmand S, Poncet S. PIV measurements of an air jet impinging on an open rotor-stator system. Exp Fluids 2012;53(2):401–12.
[42] Nguyen T, Wells J, Nguyen CV. Velocity measurement of near-wall flow over inclined and curved boundaries by extended interfacial particle image velocimetry. Flow Meas Instr 2012;23(1):33–9.
[43] Nguyen TD, Wells JC, Mokhasi P, Rempfer D. Proper orthogonal decomposition-based estimations of the flow field from particle image velocimetry wall-gradient measurements in the backward-facing step flow. Meas Sci Technol 2010;21(11) 115,406.
[44] Nguyen CV, Nguyen T, Wells J, Nakayama A. Interfacial PIV to resolve flows in the vicinity of curved surfaces. Exp Fluids 2010;48(4):577–87.
[45] Nie J, Armaly BF. Reverse flow regions in three-dimensional backward-facing step flow. Int J Heat Mass Transf 2004;47(22):4713–20.
[46] Ötügen M. Expansion ratio effects on the separated shear layer and reattachment downstream of a backward-facing step. Exp Fluids 1991;10(5):273–80.
[47] Ötügen M, Papadopoulos G, Vradis G, Muckenthaler G. Spanwise characteristics of the separated flow in a suddenly expanding duct. Exp Fluids 1993;14(3):213–6.
[48] Patankar SV, Spalding DB. A calculation procedure for heat, mass and momentum transfer in three-dimensional parabolic flows. Int J Heat Mass Transf 1972;15(10):1787–806.
[49] Perrin R, Braza M, Cid E, Cazin S, Moradei F, Barthet A, et al. Near-wake turbulence properties in the high Reynolds number incompressible flow around a circular cylinder measured by two-and three-component PIV. Flow Turbul Combust 2006;77(1):185–204.
[50] Piirto M, Karvinen A, Ahlstedt H, Saarenrinne P, Karvinen R. PIV measurements in square backward-facing step. J Fluids Eng 2007;129(8):984.
[51] Raffel M, Willert C, Wereley S, Kompenhans J. Particle image velocimetry: a practical guide. Springer-Verlag; 2007.
[52] Scarano F, Riethmuller M. Iterative multigrid approach in PIV image processing with discrete window offset. Exp Fluids 1999;26(6):513–23.
[53] Schram C, Rambaud P, Riethmuller M. Wavelet based eddy structure eduction from a backward facing step flow investigated using particle image velocimetry. Exp Fluids 2004;36(2):233–45.
[54] So R, Yuan S. Near-wall two-equation and Reynolds-stress modeling of backstep flow. Int J Eng Sci 1998;36(3):283–98.
[55] Soloff SM, Adrian RJ, Liu ZC. Distortion compensation for generalized stereoscopic particle image velocimetry. Meas Sci Technol 1997;8(12):1441.
[56] Spalart PR. Direct simulation of a turbulent boundary layer up to Rj=1410. J Fluid Mech 1988;187(1):61–98.
[57] Speziale CG, Sarkar S, Gatski TB. Modelling the pressure–strain correlation of turbulence: an invariant dynamical systems approach. J Fluid Mech 1991;227(1):245–72.
[58] Stevenson W, Thompson H, Craig R. Laser velocimeter measurements in highly turbulent recirculating flows. J Fluids Eng 1984;106:173–80.
[59] Tsai Y, Hunt J, Nieuwstadt F, Westerweel J, Gunasekaran B. Effect of strong external turbulence on a wall jet boundary layer. Flow Turbul Combust 2007;79(2):155–74.
[60] Tylli N, Kaiktsis L, Ineichen B. Sidewall effects in flow over a backward-facing step: experiments and numerical simulations. Phys Fluids 2002;14:3835.
[61] Vogel J, Eaton J. Combined heat transfer and fluid dynamic measurements downstream of a backward-facing step. J Heat Transf 1985;107(4):922–9.
[62] Westerweel J. Efficient detection of spurious vectors in particle image velocimetry data. Exp Fluids 1994;16(3):236–47.
[63] Westerweel J, Dabiri D, Gharib M. The effect of a discrete window offset on the accuracy of cross-correlation analysis of digital piv recordings. Exp Fluids 1997;23(1):20–8.
[64] Williams P, Baker A. Numerical simulations of laminar flow over a 3D backward-facing step. Int J Numer Methods Fluids 1997;24(11):1159–83.
[65] Wygnanski I, Katz Y, Horev E. On the applicability of various scaling laws to the turbulent wall jet. J Fluid Mech 1992;234(1):669–90.